Original Article

Radiosynthesis and evaluation of a carbon-11 labeled PET ligand for imaging of O-GlcNAcase

Yinlong Li^{1*}, Xin Zhou^{1*}, Zhendong Song¹, Taoqian Zhao¹, Jian Rong¹, Jiahui Chen¹, Chunyu Zhao¹, Qilong Hu¹, Xiaoyan Li¹, Chongjiao Li¹, Zhenkun Sun², Yabiao Gao¹, Jimmy S Patel^{1,3}, Ahmad Chaudhary¹, Hongjie Yuan², Steven H Liang¹

¹Department of Radiology and Imaging Sciences, Emory University, Atlanta, GA 30322, The United States; ²Department of Pharmacology and Chemical Biology, Emory University School of Medicine, Atlanta, GA 30322, The United States; ³Department of Radiation Oncology, Winship Cancer Institute of Emory University, Atlanta, GA 30322, The United States. *Equal contributors.

Received July 15, 2025; Accepted September 12, 2025; Epub October 25, 2025; Published October 30, 2025

Abstract: 0-GlcNAcase (OGA) is a key enzyme involved in regulating the dynamic cycling of 0-GlcNAc modifications on intracellular proteins. OGA has emerged as a promising therapeutic target for neurodegenerative diseases, including Alzheimer's disease. In this report, we present the radiosynthesis and preclinical assessment of a novel carbon-11 labeled positron emission tomography (PET) radioligand [11C]1 (codenamed OGA-2504) targeting OGA. The aminopyrimidine-based compound 1 and its corresponding desmethyl precursor were synthesized efficiently with good chemical yields. Radiosynthesis of [11C]1 was accomplished *via* 11C-methylation, yielding an 8% decay-corrected radiochemical yield with high purity (>98%) and high molar activity (92.5 GBq/µmol). [11C]1 exhibited moderate lipophilicity (LogD = 2.11) and excellent *in vivo* stability in serum. However, preliminary PET imaging revealed low brain uptake and slow clearance of [11C]1 in mice, suggesting a need for further structural optimization to enhance brain penetration.

Keywords: O-GlcNAcase, aminopyrimidine scaffold, positron emission tomography, radioligand

Introduction

O-linked-β-N-acetylglucosamine (O-GlcNAc) is a reversible post-translational modification (PTM) that occurs on serine and threonine residues of intracellular proteins [1-3]. This modification is precisely regulated by two enzymes: O-GlcNAc transferase (OGT), which catalyzes the attachment of GlcNAc from UDP-GlcNAc to serine/ threonine residues, and O-GlcNAcase (OGA), the sole glycosidase responsible for hydrolyzing O-GlcNAc modification in vivo [4, 5]. O-GlcNAcylation is involved in numerous cellular functions, such as transcriptional regulation, signal transduction, and stress responses [6, 7]. Disruption of O-GlcNAc cycling, particularly through aberrant OGA activity, has been associated with multiple pathological conditions including neurodegenerative diseases (e.g., Alzheimer's disease (AD) [8], cancer [9], and diabetes [10]). Recent studies have shown that O-GlcNAcylation plays a key role in regulating tau protein stability and function. This post-translational modification appears to modulate tau phosphorylation, its pathological counterpart, by competing for similar serine and threonine residues. Reduced O-GlcNAcylation has been associated with increased tau hyperphosphorylation, aggregation, and neurotoxicity, all of which are central to the formation of neurofibrillary tangles, a defining feature of AD pathology [11-13]. O-GlcNAcylation is rarely detected on aggregated tau species in brain extracts from cadavers of AD patients [14, 15]. Besides, relevant animal experiments have demonstrated that the administration of OGA inhibitors can elevate O-GlcNAcylation levels and attenuate tau hyperphosphorylation [16, 17]. Therefore, selective OGA inhibitors represent promising therapeutic candidates, and several compounds have already advanced to clinical trials, such as LY3372689 [18], MK-8719 [19], and ASN120290 [20].

Positron emission tomography (PET) is a non-invasive molecular imaging modality, which enables real-time visualization of enzyme activity and receptor binding in vivo [21, 22]. Identifying the appropriate OGA PET ligand is crucial for the effective screening of OGA inhibitors as well as for dosage optimization. To date, only a small number of OGA-targeted PET tracers have been developed for in vivo brain imaging application (Figure 1). Among them, Merck reported [18F]MK-8553 [23] as the first OGA PET radioligand, but its structure remains undisclosed. In 2020, Pike and coworkers developed two PET ligands, [11C]LSN3316612 and [18F]LSN3316612, both of which demonstrated favorable brain uptake and reversible binding kinetics in vitro and in vivo. Notably, [18F]LSN3316612 was favored for clinical translation due to its longer halflife and logistical advantages [24-26]. More recently, [11C] CH₂-BIO-1790735 was synthesized via [11C]CH₂I at the N-methyl position. However, the radiochemical yield of $[^{11}C]CH_3$ -BIO-1790735 was low (<2%, <150 MBq), and PET imaging in non-human primates (NHPs) revealed irreversible binding kinetics, limiting its translational potential [27, 28]. A single-atom substitution, replacing a nitrogen with carbon in [11C]CH3-BIO-1790735 resulted in a



Figure 1. Structures of OGA PET tracers.

Figure 2. Proposed potential OGA PET radioligand and the responding precursor.

new analog of [11C]CH3-BIO-1819578 that exhibited reversible binding and specific uptake in NHPs [28]. In addition, radiolabeling of [11C]BIO-1819578 at the carbonyl position was accomplished via one-step ¹¹C-acylation with [11C]CO [29, 30]. This ligand was also evaluated in NHP PET imaging, though the molar activity was only moderate (14 ± 5 GBq/µmol). Therefore, there is a clear need to develop new OGA radioligands with favorable imaging characteristics and strong translational potential to enable reliable in vivo quantification of OGA. While most reported OGA PET radioligands are based on chiral piperidines and exhibit high affinity, they are often limited by stereochemical complexity and metabolic stability. In contrast, the aminopyrimidine scaffold offers a structurally versatile alternative and is widely recognized as a privileged hinge-binding motif in medicinal chemistry. In this study, we performed a preliminary evaluation of a novel aminopyrimidine-based radioligand [11C]1 (codenamed OGA-2504) for PET imaging of OGA (Figure 2).

Materials and methods

General

Unless specified otherwise, all reagents, solvents, and chemicals were purchased from commercial sources and

used as received without additional purification. The chemical synthesis of compound 1 (OGA-2504) and its corresponding dimethyl precursor 9 was performed according to previously published method [31]. Nuclear magnetic resonance (NMR) spectra were acquired using a Bruker AVANCE NEO 400 MHZ spectrometer, operating at 400 MHz for proton (1H) and 100 MHz for carbon (13C) spectra. Chemical shifts (δ) are described in parts per million (ppm), referenced to tetramethylsilane (TMS) via the residual solvent signal. The following abbreviations are applied to describe peak multiplicity in the NMR data: singlet (s), doublet (d), triplet (t), quartet (q), and multiplet (m). High-performance liquid chromatography-mass spectrometry (HPLC-MS) was performed using an Agilent 6120B single quadrupole mass spectrometer equipped with an electrospray ionization (ESI) source. Analytical HPLC was carried out on an Agilent 1100 system equipped with a G1315A diode-array detector. High-resolution mass spectrometry (HRMS) was carried out on a Thermo Fisher Scientific UPLC-ESI-Q-Orbitrap MS system. All animal procedures were approved by the Institutional Animal Care and Use Committee (IACUC) of Emory University (protocols PROTO202200003 and PROTO202200076) and performed in compliance with institutional ethical guidelines. Female CD-1 mice (Charles River Laboratories; 22-24 g; 5-6 weeks old; strain code: 022) were housed in a controlled environment with a 12-hour light/dark cycle, with unrestricted access to food and water.

Chemistry

Synthesis of 2-chloro-4-(4-methylpiperidin-1-yl)pyrimidine (4): To a solution of 2,4-dichloropyrimidine 2 (5.0 g, 33.6 mmol) and 4-methylpiperidine 3 (4.0 g, 40.3 mmol) in THF (60 mL), triethylamine (TEA, 10.2 g, 100.8 mmol) was added at 25°C. The reaction was stirred at 25°C for 2 h. The reaction mixture was diluted by 100 mL water and then extracted with ethyl acetate (EtOAc, 20 mL × 3). The organic phase was then combined and dried over anhydrous Na₂SO₄. After removing the organic solvent in vacuo, 2-chloro-4-(4-methylpiperidin-1-yl)pyrimidine 4 was obtained as an off-white solid without purification (2.15 g, 30%). 1 H NMR (400 MHz, DMSO- d_6) δ 8.02 (d, J = 6.2 Hz, 1H), 6.82 (d, J = 6.2 Hz, 1H), 4.25 (m, 2H), 2.91 (t, J = 12.8 Hz, 2H), 1.67 (m, 3H), 1.04 (dt, J = 14.1, 12.2 Hz, 2H), 0.91 (d, J = 6.2 Hz, 3H).

Synthesis of N-((1-methyl-1H-imidazol-4-yl)methyl)-4-(4methylpiperidin-1-yl)pyrimidin-2-amine (1): To a solution of 2-chloro-4-(4-methylpiperidin-1-yl)pyrimidine (4) (200 mg, 0.945 mmol) and (1-methyl-1H-imidazol-4-yl)methanamine hydrochloride (5) (280 mg, 1.89 mmol) in 2-methyl-2-butanol (10 mL), K₂CO₃ (261 mg, 1.89 mmol) was added. The reaction mixture was stirred at 130°C for 24 h. The reaction mixture was poured into 100 mL water and extracted with dichloromethane (DCM, 20 mL × 3). The combined organic layers were washed with brine, dried over anhydrous Na₂SO₄, and concentrated to obtain the crude product, purified by silica gel column chromatography using ethyl acetate/methanol (90:10, v/v) as eluent to afford N-((1-methyl-1H-imidazol-4-yl)methyl)-4-(4methylpiperidin-1-yl)pyrimidin-2-amine 1 (125 mg, 46%) as an off-white solid. ¹H NMR (400 MHz, Chloroform-d) δ 7.77 (d, J = 6.4 Hz, 1H), 7.35 (d, J = 1.4 Hz, 1H), 6.85 (d, J = 1.4 Hz, 1H), 5.91 (d, J = 6.4 Hz, 2H), 4.54 (d, J = 5.6 Hz, 2H), 4.35 (d, J = 13.2 Hz, 2H), 3.63 (s, 3H), 2.83 (td, J =12.9, 2.3 Hz, 2H), 1.75 - 1.59 (m, 3H), 1.13 (dd, J = 15.2, 12.4 Hz, 2H), 0.96 (d, J = 6.3 Hz, 3H). ¹³C NMR (101 MHz, Chloroform-d) δ 161.1, 160.4, 154.3, 140.1, 136.2, 116.1, 92.4, 43.3, 38.6, 32.7, 32.3, 30.2, 20.8. LCMS (ESI): m/z, 287 [M+H]+. HRMS (ESI): exact mass calcd for $C_{15}H_{23}N_{6}$ [M+H⁺], 287.19787; found, 287.19736.

Synthesis of (1-trityl-1H-imidazol-4-yl)methanamine (7): To a solution of 1-trityl-1H-imidazole-4-carbaldehyde 6 (5 g, 14.8 mmol) in MeOH (100 mL), Raney Ni (1.7 g, 29.5 mmol) was added under nitrogen atmosphere. Then NH $_{\rm 3}$ / MeOH (2 mol/L, 100 mL) was added, and the reaction mixture was stirred at 25°C for 5 minutes. After the system was evacuated and then refilled with hydrogen, and the reaction was stirred at 45°C for 10 h. The reaction mixture was filtered to remove the catalyst. The filtrate was concentrated using a water bath to yield (1-trityl-1H-imidazol-4-yl)methanamine 7 (5.25 g, 98%) as an off-

white solid. 1 H NMR (400 MHz, DMS0- $d_{\rm e}$) δ 7.47-7.31 (m, 9H), 7.25 (d, J = 1.5 Hz, 1H), 7.15-7.02 (m, 6H), 6.72 (s, 1H), 4.04 (d, J = 61.8 Hz, 1H), 3.55 (s, 2H).

Synthesis of 4-(4-methylpiperidin-1-yl)-N-((1-trityl-1H-imidazol-4-yl)methyl)pyrimidin-2-amine (8): To a solution of (1-trityl-1H-imidazol-4-yl)methanamine 7 (250 mg, 1.18 mmol) and 2-chloro-4-(4-methylpiperidin-1-yl)pyrimidine 4 (800 mg, 2.36 mmol) in 2-methyl-2-butanol (10 mL), K₂CO₃ (346 mg, 2.36 mmol) was added. The reaction mixture was stirred at 130°C for 24 h. The mixture was poured into water and extracted with DCM (20 mL × 3). The combined organic layers were washed with brine, dried over anhydrous Na₂SO₄, and concentrated to obtain the crude product, purified by silica gel column chromatography using ethyl acetate/methanol (93/7) as eluent to give 4-(4-methylpiperidin-1-yl)-N-((1-trityl-1H-imidazol-4-yl)methyl)pyrimidin-2-amine 8 (249 mg, 41%) as an offwhite solid, which was used directly in the next step without further purification.

Synthesis of N-((1H-imidazol-4-yl)methyl)-4-(4-methylpiperidin-1-yl)pyrimidin-2-amine (9): To a solution of 4-(4-methylpiperidin-1-yl)-N-((1-trityl-1H-imidazol-4-yl)methyl)pyrimidin-2-amine 8 (200 mg, 0.389 mmol) in DCM (3 mL), TFA (1.2 mL) was added at 0°C. The reaction mixture was stirred at 25°C for 2 h. The mixture was concentrated to afford the crude product, which was purified by preparative HPLC to give N-((1H-imidazol-4-yl)methyl)-4-(4methylpiperidin-1-yl)pyrimidin-2-amine 9 (72 mg, 69%) as a white solid. 1 H NMR (400 MHz, DMSO- $d_{\rm e}$) δ 13.95 (s, 2H), 8.88 (s, 1H), 8.46 (s, 1H), 7.86 (d, J = 7.5 Hz, 1H), 7.52 (s, 1H), 6.56 (d, J = 7.6 Hz, 1H), 4.58 (d, J = 5.5 Hz, 2H), 3.02 (s, 2H), 1.72 (d, J = 11.9 Hz, 3H), 1.00 (s, 2H), 0.91 (d, J = 6.1 Hz, 3H). ¹³C NMR (101 MHz, DMSO- $d_{\rm s}$) δ 160.5, 159.0, 143.5, 134.8, 131.2, 117.1, 95.4, 35.5, 34.0, 30.5, 21.8. LCMS (ESI): m/z, 273 [M+H]+. HRMS (ESI): exact mass calcd for $C_{14}H_{21}N_{6}$ [M+H⁺], 273.18222; found, 273.18170.

Radiochemistry

[¹¹C]CO₂ (~37 GBq) produced via the ¹⁴N(p,α)¹¹C nuclear reaction (GE PETrace 880 cyclotron, 18 MeV, 10 min irradiation). Radiolabeling was carried out using an automated protocol on the GE TRACERlab™ FX2 C module. [¹¹C] CH₃I was prepared from [¹¹C]CO₂ in a cyclotron and then transferred into a reaction vial containing precursor 9 (1.0 mg), Cs₂CO₃ (5 mg), and tetraethylammonium bicarbonate (TEAB, 2 mg) in DMF (500 μL). Then, the reaction mixture was heated at 90°C for 5 min. Following methylation, an HPLC buffer (CH₃CN/H₂O = 65:35, v/v, containing 0.1% Et₃N, 2 mL) was added, and the crude product was was subjected to purification by semi-preparative HPLC using a SunFire C18 OBD Prep column (100 Å, 5 μm, 10 × 150 mm) with a flow rate of 5.0 mL/min. The product fraction containing [¹¹C]1 was collected between 12-14 minutes.

Scheme 1. Chemical synthesis of compound 1.

Measurement of LogD

The lipophilicity (LogD) of [¹¹C]1 was measured determined using a previously reported "shake-flask" method. Briefly, phosphate-buffered saline (PBS) and n-octanol were pre-saturated prior to use. A mixture of [¹¹C]1 (~20 MBq) in 3 mL PBS was mixed with 3 mL of n-octanol in a vial and vortexed for 5 minutes to allow phase partitioning. The two layers were then separated and transferred to a centrifuge tube, followed by centrifugation at 12,000 rpm for 5 minutes to ensure complete separation. Aliquots of the PBS (0.5 mL) and n-octanol (0.05 mL) layers were then collected, weighed, and their radioactivity quantified using a gamma counter (PerkinElmer Wizard). The LogD value was calculated using the following equation:

 $\label{eq:logD} LogD = Log[(radioactivity_{octanol}/weight_{octanol})/(radioactivity_{PBS}/weight_{PBS})]$

In vitro serum stability

A volume of 400 μ L of serum from mouse, rat, NHP, and human was preincubated at 37°C for 5 minutes. Subsequently, [\$^{11}\$C]1 (approximately 1.0 mCi) was then added to each sample, followed by incubation at 37°C for 15, 30, and 60 minutes. At each time point, 100 μ L portions were withdrawn and immediately mixed with 200 μ L of ice-cold acetonitrile to quench enzymatic activity. The samples were then vortexed, centrifuged at 10,000×g for 5 minutes at 4°C, and the resulting supernatants were filtered. The fractions of intact parent compound and radiometabolites were determined by radio-HPLC using a CH₃CN/H₂O = 65:35 (v/v) mobile phase containing 0.1 M ammonium formate. As a negative control, the same procedure was performed using PBS instead of serum.

Dynamic PET imaging

Dynamic PET imaging was performed using a MOLECU-BES β -CUBE scanner. CD-1 mice (5-6 weeks old) were anesthetized with 1.5% (v/v) isoflurane and maintained under anesthesia throughout the scan. [\$^{11}C]1 (approximately 0.2 mCi in 0.1 mL PBS) was administered intravenously via a tail vein catheter. Dynamic PET data was acquired over a 60-minute period. The dynamic PET images were reconstructed, and quantitative analysis were conducted using PMOD software (version 4.3).

Results

Chemistry

The synthesis of cold compound 1 started a nucleophilic aromatic substitution (SNAr) reaction between 2,4-dichloropyrimidine (2) and 4-methylpiperidine (3) at room temperature, yielding intermediate chloride 4 in 30% yield. A subsequent SNAr reaction of compound 4 with amine 5 under basic conditions afforded the target compound 1 in 46% yield (**Scheme 1**).

Compound properties

As shown in **Figure 3**, compound 1 exhibited favorable physicochemical and pharmacological properties. It has a molecular weight (MW) of 286.38 and a calculated lipophilicity (clogP) of 1.89. The logD was measured as 2.11 using "shake-flask" method, indicating moderate lipophilicity. The topological polar surface area (tPSA) was 55.59 Ų, within the optimal range for blood-brain barrier (BBB) permeability. The multiparameter optimization (MPO) score was 5.8, suggesting good central nervous system (CNS) drug-like characteristics. The predicted brain-to-plasma partition coefficient (LogBB) was -0.06, consistent with potential brain exposure. As previously reported, compound 1 also demonstrated potent in vitro target engagement, with an IC $_{50}$ value of 46 nM [31].

Radiochemistry

To enable efficient ¹¹C-labeling of compound 1, the corresponding dimethyl precursor 9 was synthesized starting from 1-trityl-1H-imidazole-4-carbaldehyde (compound 6, **Scheme 2**). Briefly, hydrogenation of 6 afforded amine 7 in 98% yield. Subsequent reaction with chloride 4 yielded compound 8 in 41% yield. Finally, removal of the trityl (Tr) protecting group gave the desired precursor 9 in 69% yield.

To improve radiochemical conversion under mild conditions, we optimized the labeling conditions by varying the base, phase-transfer catalyst, and reaction temperature. As summarized in **Table 1**, the reaction using $\mathrm{Cs_2CO_3}$ (5 mg) in DMF (500 μ L) at 65°C in the absence of a phase-transfer catalyst resulted in negligible radiochemical yield (<0.1%, Entry 1). Elevating the temperature to 90°C and

Parameters	MW ^a	clogP ^a	logD ^b	tPSA ^a	MPO score ^c	LogBB ^c	IC ₅₀ (nM) ^d
Value	286.38	1.89	2.11	55.59	5.8	-0.06	46

Figure 3. Key physicochemical and pharmacological properties of compound 1. ^aValues were calculated with ChemDraw 21.0 software. ^bMeasured by "shake-flask" method. ^cValues were predicted with ACD/labs. ^dReported value in reference [31].

Scheme 2. Chemical synthesis of precursor 9.

Table 1. Optimization of radiolabeling conditions

Entry	TEAB (mg)	Base (mg)	DMF (μL)	Temperature (°C)	Time (min)	(n.d.c.) RCY (%)
1	-	Cs ₂ CO ₃ (5 mg)	500	65	5	<0.1
2		NaOH (3 mg)	500	90	5	<0.1
3	2	NaOH (3 mg)	500	90	5	0.3
4	2	Cs_2CO_3 (5 mg)	300	90	5	1

Reactions were carried out on a GE TRACERlab™ FX2 C module using precursor 9 (1.0 mg).

switching the base to NaOH (3 mg) did not improve the yield significantly (Entry 2). Notably, the inclusion of tetraethylammonium bicarbonate (TEAB, 2 mg) under otherwise identical conditions led to a modest increase in yield (0.3%, Entry 3), highlighting the importance of phase-transfer catalysis. Further enhancement was achieved by reducing the reaction volume to 300 μL and using Cs_2CO_3 as the base, resulting in a non-decay-corrected (n.d.c.) radiochemical yield of 1.0% (Entry 4). These findings indicate that both the presence of TEAB and increased reagent concentration are key factors for facilitating efficient radiolabeling. Further optimization was not pursued since we could obtain sufficient activity for in vitro and in vivo studies in rodents.

$$\begin{array}{c} [^{11}\text{C}]\text{CO}_2 \\ \downarrow^{\text{H}_2} \\ \downarrow^{\text{I}^{11}\text{C}]\text{CH}_4} \\ \downarrow^{\text{I}_2} \\ \downarrow^{\text{I}_3} \\ \downarrow^{\text{I}_2} \\ \downarrow$$

Under optimized conditions, the radiosynthesis of [11 C]1 was achieved by treatment with Cs $_2$ CO $_3$ and TEAB at 90°C for 5 minutes. The product fraction containing [11 C]1 was collected between 12 and 14 minutes. [11 C]1 was obtained in an 8% decay-corrected RCY based on [11 C]

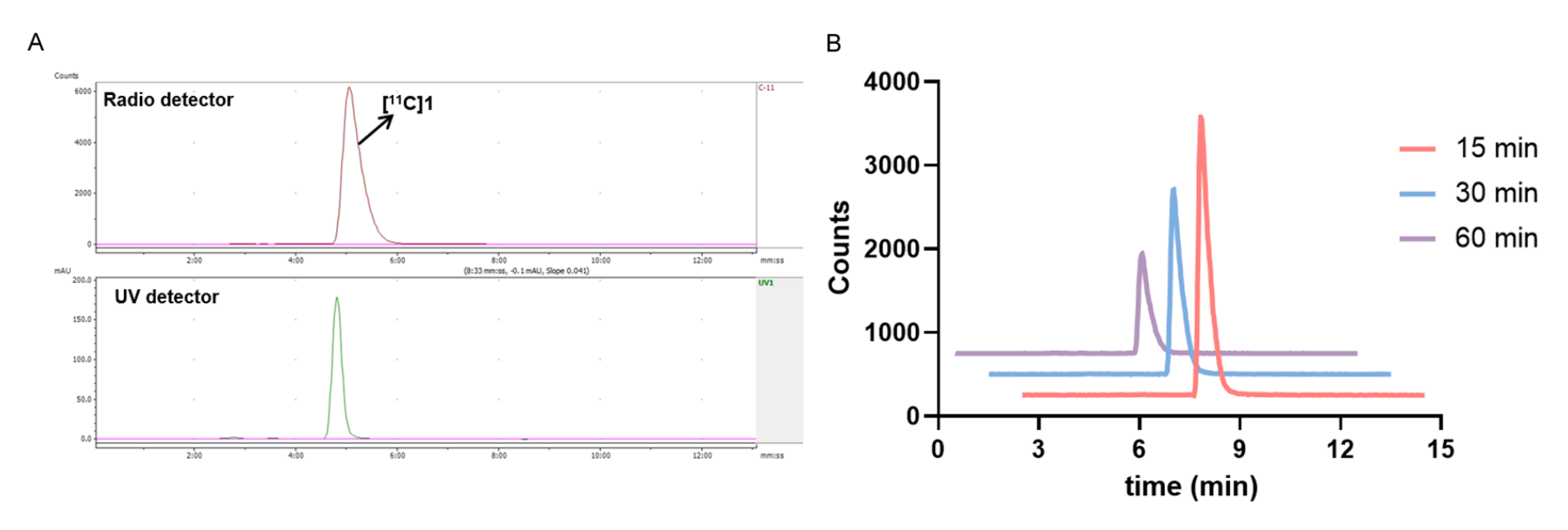


Figure 4. A. Representative radio-HPLC chromatogram confirming the identity of [11C]1 by co-injection with reference compound 1. B. Formulation stability analysis of [11C]1 in PBS.

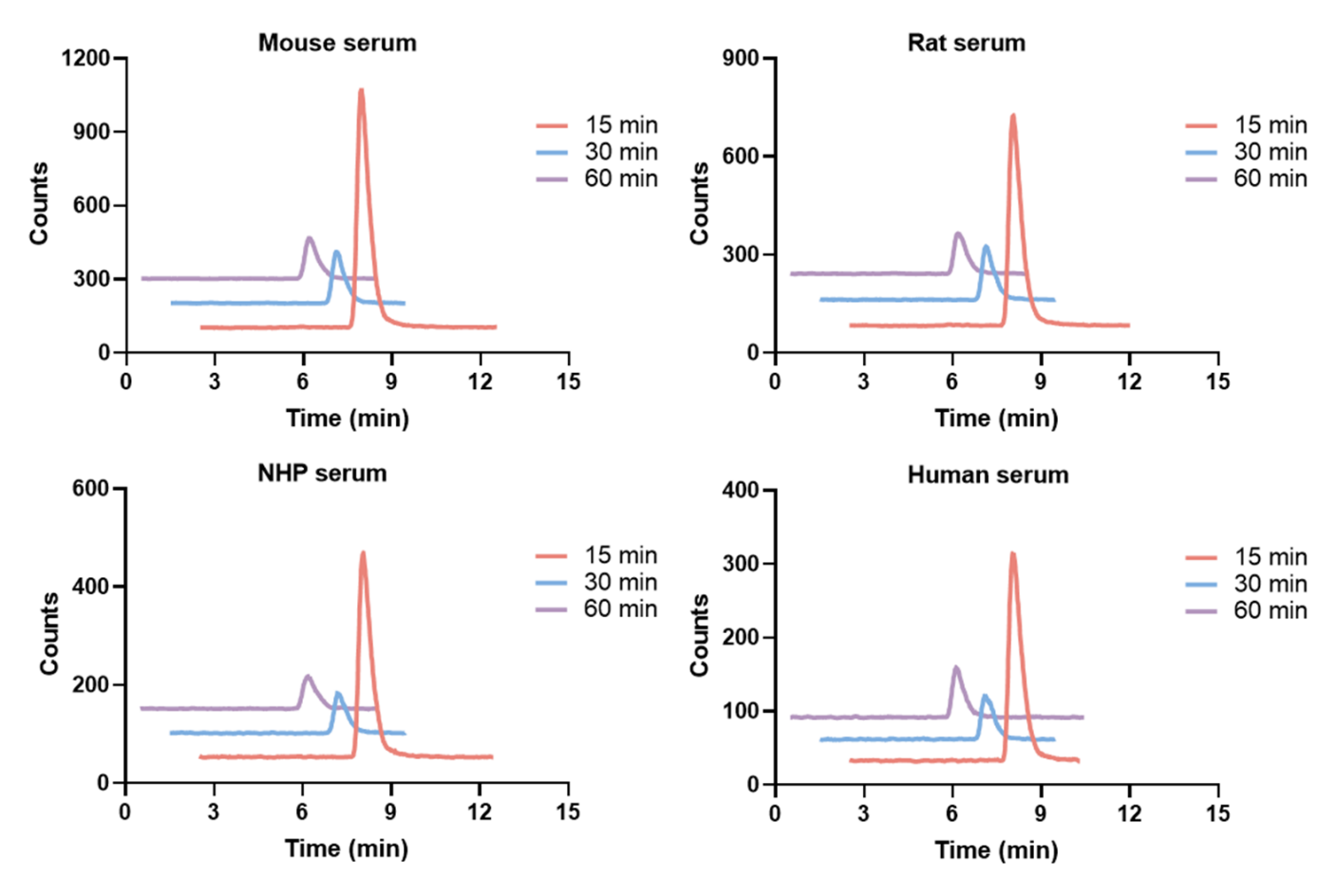


Figure 5. HPLC analysis of [11C]1 incubated with serums from humans and different animal species.

 ${\rm CO}_2$, with high radiochemical purity (>98%) and molar activity (92.5 GBq/ μ mol).

In vitro stability

The radiolabeled compound [¹¹C]1 was identified by coinjection with the non-radioactive reference compound 1 (Figure 4A). The formulation stability of [¹¹C]1 in PBS was evaluated at 15, 30, and 60 minutes post-incubation, and no radiolabeled metabolites were detected (Figure 4B). We also evaluated the in vitro stability of [¹¹C]1 in serum from mouse, rat, NHP, and human. The tracer remained highly stable for up to 60 minutes in all species (Figure 5).

In vivo PET imaging study

As shown in **Figure 6A**, dynamic *in vivo* PET imaging study was performed in CD-1 mice over 0-60 minutes. [11C]1 exhibited low and homogeneous brain uptake, with slow clearance observed across major brain regions (**Figure 6B-D**).

Discussion

To date, few PET radioligands targeting OGA have been reported, and most of them share a highly similar struc-

tural framework based on chiral piperidine scaffolds. While these radioligands have demonstrated promising imaging potential, the chemical diversity among available OGA tracers remains narrow, potentially limiting advances in selectivity, pharmacokinetics, and translational applications. In this study, we aimed to evaluate a structurally distinct aminopyrimidine-based [¹¹C]1, as a novel PET tracer for imaging OGA. Compound 1 was identified through a virtual screening strategy that integrated both structure-based and ligand-based approaches [31]. The synthesis of compound 1 was straightforward, accomplished in two steps from commercially available 2,4-dichloropyrimidine (2) and 4-methylpiperidine (3), with an overall yield of 13.8% (Scheme 1).

In silico calculations predicted favorable physicochemical and pharmacological properties for PET tracer development. Compound 1 has a molecular weight of 286.38, a calculated clogP of 1.89, and an experimentally measured logD of 2.11, which is within the ideal range for achieving effective BBB penetration while minimizing non-specific binding. Other physicochemical parameters of compound 1 (TPSA = 55.89 Å^2 ; MPO = 5.8; logBB = -0.06) also support its potential for brain permeability. These parameters are consistent with those previously reported OGA-targeted radiotracers. For instance, LSN3316612 and BIO1819578 were structurally opti-

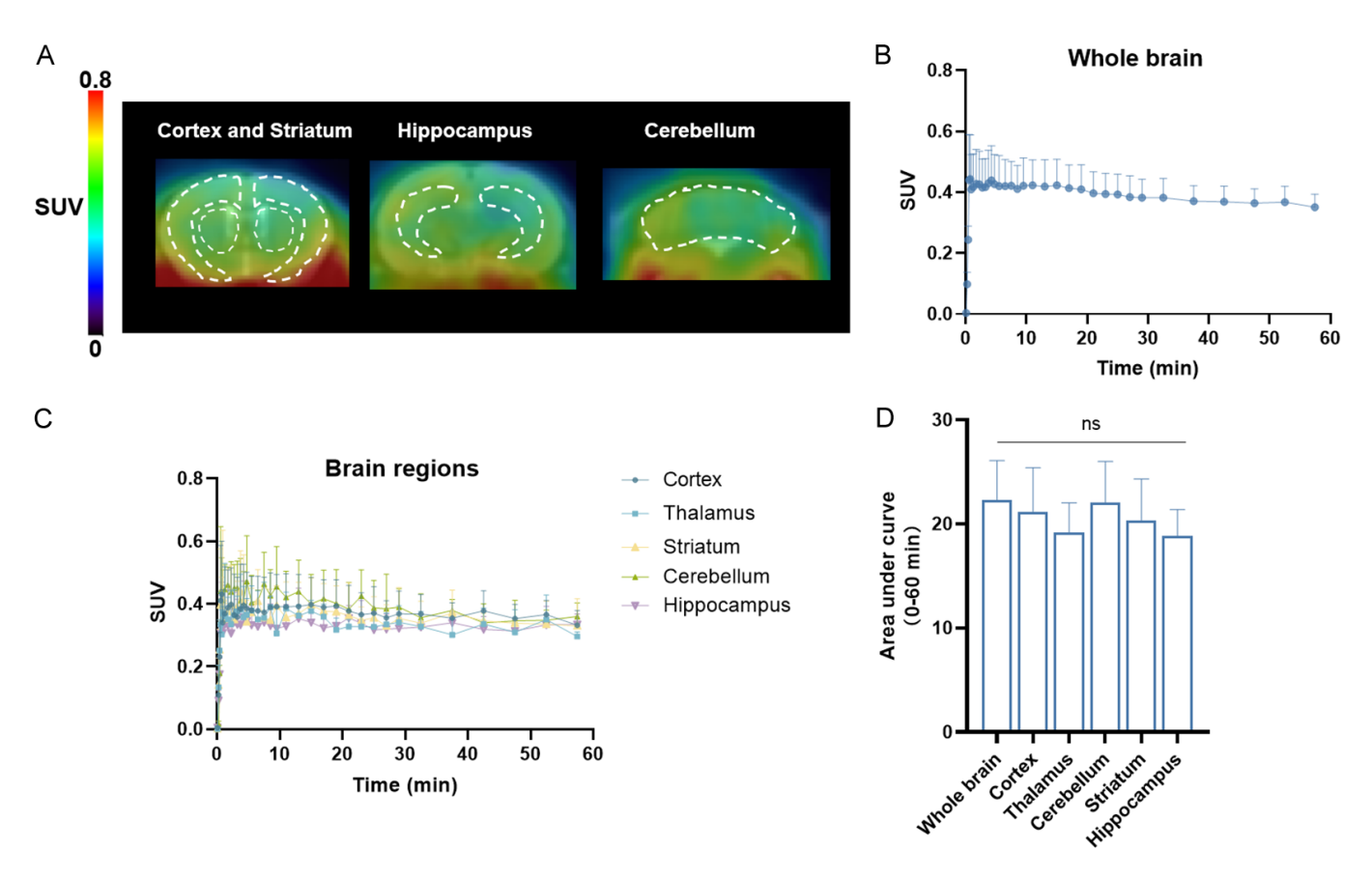


Figure 6. A. Summed PET images (0-60 min) [11 C]1 in CD-1 mouse brains under baseline conditions. B. Time-activity curve (TAC) of [11 C]1 in the whole brain. C. TACs in selected brain regions of interest. D. Area under the curve (AUC, 0-60 min) analysis. N = 3. Ns = Not significant.

mized to balance polarity and lipophilicity, achieving TPSA values below 70 Å² to favor BBB permeability. Importantly, compound 1 also exhibits high in vitro binding affinity toward OGA, with an $\rm IC_{50}$ value of 46 nM [31]. Although this is higher than that of BIO1819578 (IC_{50} : 5 nM), it remains sufficient for PET imaging. However, comparison with potent OGA inhibitors such as MK-8719 and LY3372689 highlights structure-activity relationship (SAR) features absent in OGA-2504. MK-8719 incorporates two hydroxyl groups that form strong hydrogen bonds within the active site, whereas LY3372689 employs a chiral heteroaryl-piperidine scaffold with fluorine substitution to enhance lipophilicity and hydrogen bonding. OGA-2504 exhibits weaker potency, likely due to insufficient polar substituents and limited hydrophobic interactions. These insights suggest that introducing additional polar groups and lipophilic substituents may improve its affinity for the enzyme active site.

Optimization of the C-11 radiolabeling conditions was critical to achieving acceptable radiochemical yields. The final radiosynthesis protocol incorporated TEAB as a phase-transfer catalyst, which significantly improved radiochemical conversion compared to reactions using inorganic bases. Under these optimized conditions, [11 C]1 was obtained in a decay-corrected RCY of 8%, (molar activity = 92.5 GBq/ μ mol), which is compatible with other

carbon-11-labeled OGA tracers. These values are within the acceptable range for preclinical imaging studies and demonstrate the practical feasibility of producing [¹¹C]1. In addition, [¹¹C]1 demonstrated excellent formulation stability in PBS, with no radiolabeled metabolites detected up to 60 minutes post-incubation (Figure 4B). This favorable stability profile was further verified *in vitro* across multiple species, including mouse, rat, NHP, and human serum. In all cases, the tracer remained highly stable for up to 60 minutes, indicating robust plasma resistance and metabolic integrity that is an essential feature for reliable *in vivo* imaging and quantification (Figure 5).

Despite its promising physicochemical properties and high *in vitro* stability, the *in vivo* PET imaging results revealed limitations. As shown in the dynamic PET imaging study in CD-1 mice (**Figure 6**), [11C]1 exhibited low and homogeneous brain uptake, with limited regional differentiation. Furthermore, the tracer displayed slow clearance, which could indicate suboptimal brain penetration or insufficient target engagement under baseline conditions. These discrepancies between *in vitro* properties and *in vivo* performance may be attributed to factors such as high plasma protein binding or active efflux. These findings highlight the need for further SAR optimi-

zation to improve brain permeability and enhance specific binding *in vivo*.

Conclusion

In this study, we synthesized and evaluated a novel aminopyrimidine-based PET radioligand [11C]1 for imaging OGA. [11C]1 was obtained via [11C]methylation with 8% decay-corrected RCY. The tracer showed excellent in vitro stability and favorable physicochemical properties predictive of brain permeability. However, in vivo PET imaging studies in CD-1 mice revealed low and uniform brain uptake, along with slow clearance, suggesting limited brain penetration or target engagement. Despite these limitations, this work provides a new scaffold and valuable insights for further optimization of aminopyrimidinebased OGA PET tracers. Future SAR optimization should focus on modifying lipophilicity, introducing polar substituents, or adjusting hydrogen-bonding patterns to enhance brain penetration. Computational modeling could further support these structural modifications and accelerate the design of improved analogs.

Acknowledgements

We thank Emory Center for Systems Imaging Radiopharmacy (Ronald J. Crowe, RPh, BCNP; Karen Dolph, RPh; M. Shane Waldrep) & Department of Radiology and Imaging Sciences, Emory University School of Medicine for general support. We also thank Emory Center for Systems Imaging for assistance with small animal micro-PET/CT system, which was funded by the NIH grant (S100D034326) and Emory Integrated Core Facilities.

Disclosure of conflict of interest

None.

Address correspondence to: Yinlong Li and Steven H Liang, Department of Radiology and Imaging Sciences, Emory University, Atlanta, GA 30322, The United States. E-mail: yinlong.li@emory.edu (YLL); steven.liang@emory.edu (SHL)

References

- [1] Torres CR and Hart GW. Topography and polypeptide distribution of terminal N-acetylglucosamine residues on the surfaces of intact lymphocytes. Evidence for O-linked GlcNAc. J Biol Chem 1984; 259: 3308-17.
- [2] Haltiwanger RS, Holt GD and Hart GW. Enzymatic addition of O-GlcNAc to nuclear and cytoplasmic proteins. Identification of a uridine diphospho-N-acetylglucosamine:peptide beta-N-acetylglucosaminyltransferase. J Biol Chem 1990; 265: 2563-8.
- [3] Hanover JA. Glycan-dependent signaling: O-linked N-acetylglucosamine. FASEB J 2001; 15: 1865-76.
- [4] Nagel AK and Ball LE. O-GlcNAc transferase and O-GlcNAcase: achieving target substrate specificity. Amino Acids 2014; 46: 2305-16.

- [5] Yang X and Qian K. Protein O-GlcNAcylation: emerging mechanisms and functions. Nat Rev Mol Cell Biol 2017; 18: 452-65.
- [6] Zachara NE and Hart GW. The emerging significance of O-GlcNAc in cellular regulation. Chem Rev 2002; 102: 431-8
- [7] Ong Q, Han W and Yang X. O-GlcNAc as an integrator of signaling pathways. Front Endocrinol (Lausanne) 2018; 9: 599.
- [8] Wani WY, Chatham JC, Darley-Usmar V, McMahon LL and Zhang J. O-GlcNAcylation and neurodegeneration. Brain Res Bull 2017; 133: 80-7.
- [9] Ferrer CM, Sodi VL and Reginato MJ. O-GlcNAcylation in cancer biology: linking metabolism and signaling. J Mol Biol 2016; 428: 3282-94.
- [10] Ma J and Hart GW. Protein O-GlcNAcylation in diabetes and diabetic complications. Expert Rev Proteomics 2013; 10: 365-80.
- [11] Lee VM, Goedert M and Trojanowski JQ. Neurodegenerative tauopathies. Annu Rev Neurosci 2001; 24: 1121-59.
- [12] Arnold CS, Johnson GW, Cole RN, Dong DLY, Lee M and Hart GW. The microtubule-associated protein tau is extensively modified with O-linked N-acetylglucosamine. J Biol Chem 1996; 271: 28741-4.
- [13] Gatta E, Lefebvre T, Gaetani S, Dos Santos M, Marrocco J, Mir AM, Cassano T, Maccari S, Nicoletti F and Mairesse J. Evidence for an imbalance between tau O-GlcNAcylation and phosphorylation in the hippocampus of a mouse model of Alzheimer's disease. Pharmacol Res 2016; 105: 186-97.
- [14] Liu F, Iqbal K, Grundke-Iqbal I, Hart GW and Gong CX. O-GlcNAcylation regulates phosphorylation of tau: a mechanism involved in Alzheimer's disease. Proc Natl Acad Sci U S A 2004; 101: 10804-9.
- [15] Sato Y, Naito Y, Grundke-Iqbal I, Iqbal K and Endo T. Analysis of N-glycans of pathological tau: possible occurrence of aberrant processing of tau in Alzheimer's disease. FEBS Lett 2001; 496: 152-60.
- [16] Hastings NB, Wang X, Song L, Butts BD, Grotz D, Harg-reaves R, Fred Hess J, Hong KK, Huang CR, Hyde L, Laverty M, Lee J, Levitan D, Lu SX, Maguire M, Mahadom-rongkul V, McEachern EJ, Ouyang X, Rosahl TW, Selnick H, Stanton M, Terracina G, Vocadlo DJ, Wang G, Duffy JL, Parker EM and Zhang L. Inhibition of O-GlcNAcase leads to elevation of O-GlcNAc tau and reduction of tauopathy and cerebrospinal fluid tau in rTg4510 mice. Mol Neurodegener 2017; 12: 39.
- [17] Rostgaard N, Jul PH, Garmer M and Volbracht C. Increasing O-GlcNAcylation attenuates tau hyperphosphorylation and behavioral impairment in rTg4510 tauopathy mice. J Integr Neurosci 2023; 22: 135.
- [18] Kielbasa W, Goldsmith P, Donnelly KB, Nuthall HN, Shcherbinin S, Fleisher AS, Hendle J, DuBois SL, Lowe SL, Zhang FF, Woerly EM, Dreyfus NJ, Evans D, Gilmore J, Mancini M, Constantinescu CC, Gunn RN, Russell DS, Collins EC, Brys M, Hutton ML and Mergott DJ. Discovery and clinical translation of ceperognastat, an O-GlcNAcase (OGA) inhibitor, for the treatment of Alzheimer's disease. Alzheimers Dement (N Y) 2024; 10: e70020.
- [19] Selnick HG, Hess JF, Tang C, Liu K, Schachter JB, Ballard JE, Marcus J, Klein DJ, Wang X, Pearson M, Savage MJ, Kaul R, Li TS, Vocadlo DJ, Zhou Y, Zhu Y, Mu C, Wang Y, Wei Z, Bai C, Duffy JL and McEachern EJ. Discovery of MK-

- 8719, a potent O-GlcNAcase inhibitor as a potential treatment for tauopathies. J Med Chem 2019; 62: 10062-97.
- [20] Ryan JM, Quattropani A, Abd-Elaziz K, den Daas I, Schneider M, Ousson S, Neny M, Sand A, Hantson J, Permanne B, Wiessner C and Beher D. Phase 1 study in healthy volunteers of the O-GlcNAcase inhibitor ASN120290 as a novel therapy for progressive supranuclear palsy and related tauopathies. Alzheimers Dement 2018; 14: P251.
- [21] Deng X, Rong J, Wang L, Vasdev N, Zhang L, Josephson L and Liang SH. Chemistry for positron emission tomography: recent advances in ¹¹C-, ¹⁸F-, ¹³N-, and 1⁵O-labeling reactions. Angew Chem Int Ed Engl 2019; 58: 2580-605.
- [22] Rong J, Haider A, Jeppesen TE, Josephson L and Liang SH. Radiochemistry for positron emission tomography. Nat Commun 2023; 14: 3257.
- [23] Li W, Salinas C, Riffel K, Miller P, Zeng Z, Lohith T, et al. The discovery and characterization of [18F]MK-8553, a novel PET tracer for imaging O-GlcNAcase (OGA). 11th International Symposium on Functional NeuroReceptor Mapping of the Living Brain, 2016, Book O-001.
- [24] Lu S, Haskali MB, Ruley KM, Dreyfus NJ, DuBois SL, Paul S, Liow JS, Morse CL, Kowalski A, Gladding RL, Gilmore J, Mogg AJ, Morin SM, Lindsay-Scott PJ, Ruble JC, Kant NA, Shcherbinin S, Barth VN, Johnson MP, Cuadrado M, Jambrina E, Mannes AJ, Nuthall HN, Zoghbi SS, Jesudason CD, Innis RB and Pike VW. PET ligands [18F]LSN3316612 and [11C]LSN3316612 quantify O-linked-β-N-acetyl-glucosamine hydrolase in the brain. Sci Transl Med 2020; 12: eaau2939.
- [25] Lee JH, Liow JS, Paul S, Morse CL, Haskali MB, Manly L, Shcherbinin S, Ruble JC, Kant N, Collins EC, Nuthall HN, Zanotti-Fregonara P, Zoghbi SS, Pike VW and Innis RB. PET quantification of brain O-GlcNAcase with [18F]LSN3316612 in healthy human volunteers. EJNMMI Res 2020; 10: 20.

- [26] Lee JH, Veronese M, Liow JS, Morse CL, Montero Santamaria JA, Haskali MB, Zoghbi SS, Pike VW, Innis RB and Zanotti-Fregonara P. Region- and voxel-based quantification in human brain of [18F]LSN3316612, a radioligand for O-GIcNAcase. EJNMMI Res 2021; 11: 35.
- [27] Nag S, Arakawa R, Datta P, Morén A, Varrone A, Moein MM, Bolin M, Lin E, Genung N and Martarello L. Synthesis and biological evaluation of a novel radioligand [11C]BIO-1790735 for detection of O-GlcNAcase (OGA) enzyme activity. Int J Nucl Med Biol 2022; 108: S26.
- [28] Cook BE, Nag S, Arakawa R, Lin EY, Stratman N, Guckian K, Hering H, Lulla M, Choi J, Salinas C, Genung NE, Morén AF, Bolin M, Boscutti G, Plisson C, Martarello L, Halldin C and Kaliszczak MA. Development of a PET tracer for OGA with improved kinetics in the living brain. J Nucl Med 2023; 64: 1588.
- [29] Nag S, Bolin M, Datta P, Arakawa R, Forsberg Morén A, Khani Maynaq Y, Lin E, Genung N, Hering H, Guckian K, Martarello L, Kaliszczak M and Halldin C. Development of a novel [11C]CO-labeled positron emission tomography radioligand [11C]BIO-1819578 for the detection of O-GlcNAcase enzyme activity. ACS Chem Neurosci 2023; 14: 2560-8
- [30] Bolin M, Nag S, Arakawa R, Varrone A, Farde L, Martarello L, Kaliszczak MA, Halldin C and Morén AF. In vivo quantification of [11C]BIO-1819578 in non-human primates, a novel radioligand for O-GlcNAcase. J Cereb Blood Flow Metab 2025; 45: 1606-1616.
- [31] Tawada M, Fushimi M, Masuda K, Sun H, Uchiyama N, Kosugi Y, Lane W, Tjhen R, Endo S and Koike T. Discovery of a novel and brain-penetrant O-GlcNAcase inhibitor via virtual screening, structure-based analysis, and rational lead optimization. J Med Chem 2021; 64: 1103-15.